Paper ID ILASS08-1-6

ILASS 2008
Sep. 8-10, 2008, Como Lake, Italy

EXPERIMENTAL INVESTIGATION OF THE CORRELATION BETWEEN NOZZLE FLOW AND SPRAY USING LDV, PDA, HIGH-SPEED PHOTOGRAPHY AND X-RAY RADIOGRAPHY

Benjamin Balewski*, Barbara Heine** and Cameron Tropea°

*Robert Bosch GmbH, Corporate Research, Gerlingen, Germany, benjamin.balewski@de.bosch.com
**Robert Bosch GmbH, Corporate Research, Gerlingen, Germany, barbara.heine@de.bosch.com
°Chair of Fluid Mechanics and Aerodynamics, Technische Universitaet Darmstadt, Darmstadt, Germany, ctropea@sla.tu-darmstadt.de

ABSTRACT

This paper presents experimental investigations of the nozzle flow and spray in a pressure atomizer. Different inlays in the nozzle were used to modify the nozzle flow. To isolate the influence of turbulence and cross-flow velocity on the primary atomization, an operating point without cavitation in the nozzle was selected. This was monitored using a high-speed camera in combination with a long distance microscope. Inside the transparent nozzle a two-velocity component laser Doppler velocimeter (LDV) was used to measure velocity and turbulence distributions at the nozzle exit. For the characterisation of the spray, different measurement techniques have been applied: high-speed photography to determine the spray angle, a phase Doppler system (PDA) for the velocity distribution and droplet sizes in the spray, and X-ray radiography for the spray angle and to evaluate the liquid density distribution. Finally, the correlations between the flow characteristics in the nozzle and the spray characteristics are discussed using the experimental results.

1 INTRODUCTION

For the simulation of primary atomization and the correct prediction of spray characteristics in for example diesel nozzles, the relevant physical processes have to be identified and properly modelled. To understand these processes three basic experimental approachs have been used: investigations with real nozzles, but here the high velocities and the small dimensions make the measurements very challenging; the second approach is to use scaled-up models, and the third is to investigate small nozzles with simplified geometries.

Using the third approach Tamaki and Shimizu [1] and Hiroyasu [2] demonstrated the strong influence of nozzle geometry on the primary spray breakup. They found breakup at relatively low pressures for small inlet radii and a short orifice length, attributing this to cavitation and increased turbulence. In an enlarged nozzle with a 90° angle between approach channel and orifice Ganippa et al. [3] found an improved breakup on the side of the spray where cavitation occurred in the nozzle. Sou et al. [4] found a connection between a collapsing cavitation cloud and the appearance of a ligament in the breakup zone. Badock [5] postulated that the turbulence generated in the cavitation area was responsible for promoting breakup. Also Stahl et al. [6] found enhanced spray breakup with the occurance of very small cavitation bubbles. The idea that a low turbulence level stabilizes a jet whereas high turbulence levels, especially in the cross-flow direction, are necessary for an improved breakup was developed by Heukelbach [7] and Walter [8].

To separate the effects of cavitation and turbulence the present paper compares four different nozzle geometries at an operating point where no cavitation exists. After a short presentation of the experimental facility the employed measurement techniques are explained with an emphasis on the X-ray tomography. Then the results of the measurements inside the nozzle are examined with respect to the measurements in the spray.

2 EXPERIMENTAL SETUP

2.1 Experimental facility

For the present measurements we used a hydraulic system (shown in Fig. 1) which operates with a constant volume flux of $q = 2.0\,l/min$ and a constant temperature of $T = 300\,K$. Before the nozzle the pressure is about $p = 1.7 \pm 0.2\,MPa$, depending on the actual nozzle geometry. In the Ohnesorge diagram this operating point is in the atomization regime. This system has been described in detail by Stahl et al. [6].

The laser Doppler measurements inside the Plexiglas nozzle require a liquid, which has the same refractive index as the Plexiglas. The physical data for the liquid used in this study are given in Table 1.

For the X-ray measurements an additional shielding made of $30\,mm$ Plexiglas on the sides and $5\,mm$ brass before and after the X-ray source is mounted for radiation protection. Furthermore, the focal spot of the X-ray source was surrounded by a $5\,mm$ lead plate with a small hole where the radiation is emitted.

Tab. 1: Physical properties for Shell Gravex 917 at $T = 300\,K$.

Density	refractive index	kin. viscosity	surface tension
$898\,\frac{kg}{m^3}$	1.49	$18\,\frac{mm^2}{s}$	$29.5 \cdot 10^{-3}\,\frac{N}{m^2}$

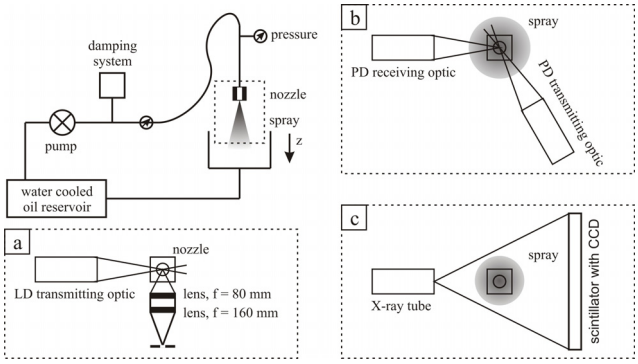

Fig. 1: Measurement facility with the setup for LDV (a), PDA (b) and X-ray-measurements (c).

2.2 Nozzle design

To investigate different nozzle geometries an axially symmetric reference nozzle was used, in which different inlays made of Plexiglas could be placed. The reference nozzle has an approach diameter of $D = 10\,mm$, a nozzle diameter of $d = 1\,mm$, an inlet radius of $r_i = 150\,\mu m$ and an orifice length of $L = 10\,mm$.
Three different inlays were designed to produce a flow field which is similar to that of a real diesel nozzle (Fig. 2). These inlays can be placed in the approach channel of the reference nozzle with a fixed gap to the orifice inlet. This system makes it convenient to obtain different inflow conditions in the orifice. The reference nozzle is referred to as VD and the three nozzle inlays are called V3, V4 and V5 respectively.
The investigated operating point of $q = 2.0\,l/min$ volume flux, corresponding to a Reynolds number of $Re = 2300$, was chosen because using inlay V5, cavitation occured at the orifice inlet at volume fluxes above $2.5\,l/min$. This was determined from high-speed images of the nozzle inlet flow using a long distance microscope.

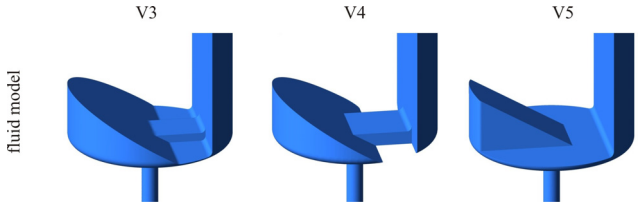

Fig. 2: Design of nozzle inlays V3, V4 and V5 with the resulting fluid model.

2.3 High-speed photography

For an initial characterisation of the spray, high-speed images have been made. As seen in Figure 3 significantly different sprays are obtained for each inlay at the same operating point. The goal is to examine the nozzle flow and to identify what differences in flow characteristics are responsible for the differences in spray breakup.

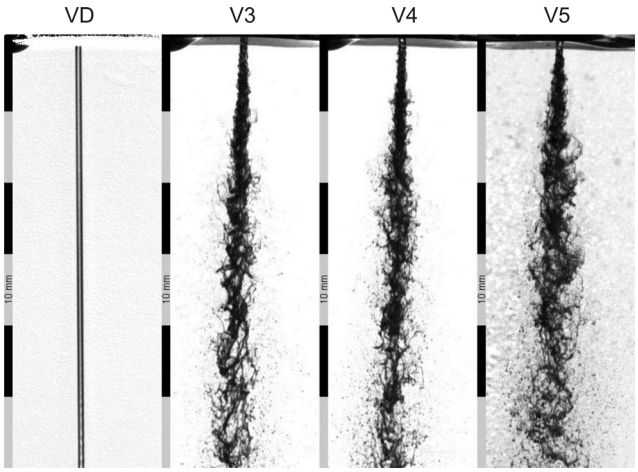

Fig. 3: High-speed images of spray resulting from the reference nozzle VD and the inlay V3, V4 and V5. Exposure time: $5\,\mu s$. Operating Point: $Re = 2300$.

2.4 Flow measurements inside the nozzle

For the flow measurements inside the nozzle a laser Doppler system was used. The setup is shown in Figure 1a. To obtain suitable spatial resolution inside the nozzle of diameter $d = 1\,mm$ we have used a two-velocity component DANTEC X55 optic with two beam expanders to first create a small, well focused illumination volume of diameter $50\,\mu m$. A receiving optics in side scatter mode ($\vartheta_{LD} = 90°$) with a magnification of two and a pinhole of $50\,\mu m$ diameter was used to truncate the detection volume to a diameter of $25\,\mu m$ and length of $50\,\mu m$. Measuring in a grid of $50 \times 50\,\mu m$ there are theoretically 313 points in a plane across the nozzle. In practice we can measure about 280 points. This is due to reflections in the regions near the wall, which result in higher measurement uncertainty.
After all grid points in a plane are measured the nozzle is rotated $90°$ and all grid points are again measured. This is necessary to obtain three components of velocity with a two-velocity component laser Doppler system.
At each point two values for the axial velocity values are available as well as the velocity values in the x- and y-directions perpendicular to the flow direction. In the subsequent evaluation the mean of the two axial velocities is taken.

2.5 System noise and spatial correction of the LDV measurements

System noise. The system noise of the LDV system results in increased measured velocity fluctuations (RMS). To identify the magnitude of this increase or 'apparent turbulence', Fischer [9] assumed a linear correlation between the RMS and the mean velocity:

$$\overline{u'^2_{noise}} = a + b \cdot \overline{u}^2 \qquad (1)$$

The coefficients in Eq. (1) can be estimated from measurements in a laminar flow at different Reynolds numbers, where all measured fluctuations can be attributed to apparent turbulence. This procedure has been used and the resulting coefficients for both velocity channels are shown in Table 2. The LDV system operates in coincident mode with the blue channel as master.

Tab. 2: Coefficients for the system noise correction of RMS for the two-velocity component LDV system calculated from measurements at Reynolds numbers between 150 and 600 in the center of a laminar channel flow.

channel	$a\left[\frac{m^2}{s^2}\right]$	$b\,[-]$
blue, axial velocity	0.000278	0.000287
green, cross velocity	0.085734	0.000154

Spatial correction. In areas with strong spatial gradients a bias of velocity and RMS occurs due to the finite size of the LDV detection volume. A second-order correction is given in Albrecht et al. [10] for a velocity gradient in one direction. The term for the correction of velocity is very small for the present system and therefore negligible. However the assumption of only one relevant velocity gradient is not correct. Therefore the correction has been expanded to include a second velocity gradient:

$$\overline{u'^2}\,(x_0,y_0) = \overline{u'^2_m}\,(x,y) - \frac{d_m^2}{12}\frac{d\overline{u}(x,y)}{dx}\bigg|^2_{x=x_0} - \frac{l_m^2}{12}\frac{d\overline{u}(x,y)}{dy}\bigg|^2_{y=y_0} \quad (2)$$

In Figure 4 the effect of the gradient correction on the axial RMS is shown. For the gradient in x-direction (0°,180°the diameter $d_m = 25\,\mu m$ and for the y-direction the length $l_m = 50\,\mu m$ of the measurement volume is taken. The predominant velocity gradient for these profiles is along the the length of the measurement volume; hence little effect is seen by the correction. In the profiles at 90° and 270° (y-direction) the correction has a relatively strong influence because here the main gradient is also in the y-direction.

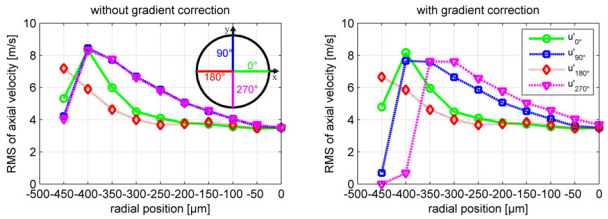

(a) (b)

Fig. 4: Comparison of axial RMS with (a) and without (b) gradient correction for inlay V5.

2.6 Spray measurements: Phase Doppler measurements

To obtain information about the velocity and drop size distribution in the spray a phase Doppler system from Dantec Dynamics was used (Figure 1). The system operates at an off-axis angle of $\vartheta_{PDA} = 60°$ (first-order refraction) and with a slit-size of $b_{slit} = 100\,\mu m$.
The measurements were performed $60\,mm$ from the nozzle exit on the axis of the coordinate system shown in Figure 7 with a step size of $1\,mm$.

2.7 Spray measurements: X-ray radiography

For evaluating the density distribution in the near nozzle region, where optical access is very restricted, an X-ray system has been developed. The configuration of this system is shown in Figure 1: an X-ray tube is placed on one side of the spray and on the opposite side there is a scintillator followed by an CCD-camera. The scintillator transforms the X-rays into visible light that can be detected by the CCD-sensor.
The selected operating point of the X-ray tube is $8\,kV$ at $0.191\,mA$. These are very low values for the X-ray tube, but they are necessary to receive a weak radiation that will be measurably attenuated in the thin spray regions. To acquire one final X-ray image twenty single pictures with an exposure time of fifteen seconds each were averaged.

3 EVALUATION OF THE X-RAY MEASUREMENTS

3.1 Intensity distribution

For the generation of an X-ray image the following steps have to be followed. First an X-ray image from the spray with the intensity distribution I is made. Than a second image with the intensity distribution I_0 with no object between the X-ray tube and camera is made. This sequence must be followed because the system gets contaminated by oil mist during the measurement with the spray. The obscuration from the deposited oil films is therefore accounted for in the measured reference intensity. Then the first image is divided by the second resulting in an image with the intensity ratio $\frac{I}{I_0}$. A value of 1.0 means that there is no medium in the line from the X-ray source to the detector.
For the next steps we assume that the Lambert-Beer law

$$I\,(r,\Theta) = I_0 e^{\int \mu(x,y)ds} \quad (3)$$

describes the attenuation of the radiation on the way ds through a medium with the spatially dependent attenuation coefficient $\mu(x,y)$, where $\mu(x,y)$ is a product of the actual density $\rho(x,y)$ on the attenuation coefficient $\overline{\mu}_{medium}$.

3.2 Absorption coefficient and scale

The absorption coefficient and the image scale are determined from an X-ray image from a solid liquid jet, which is generated by the nozzle VD with low volume flux and pressure. Supposing we are near the nozzle exit, the diameter of the jet is equal to that of the nozzle exit.

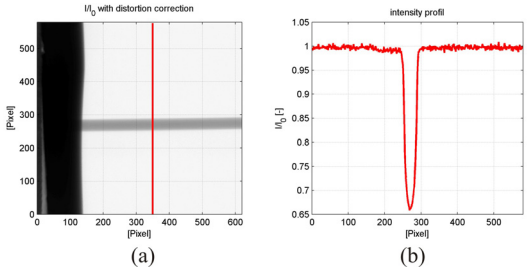

(a) (b)

Fig. 5: X-ray image from a liquid jet with nozzle on the left side (a) and intensity profile through the jet (b).

After a distortion correction and the calculation of the intensity ratio we take a line out of the image. This represents an intensity

profile across the jet. Neglecting the absorption of the surrounding air the lowest amplitude of this profile corresponds to the longest effective path length through the jet, which is equal to the known diameter of the nozzle. With Eq. (3) the absorption coefficient than can be evaluated as

$$\overline{\mu}_{medium} = 0.434 \pm 0.002 \, \frac{m^2}{kg}. \tag{4}$$

The determination of the image scaling is also possible with these images or rather the intensity profiles. Starting at the position of the minimum amplitude of a profile the area between 1.0 and the profile is calculated stepwise by adding a pixel left and right. If the so received area is equal to the theoretical area under a profile of a $1\,mm$ jet the calculation is stopped; then the distance between the left and right pixel number divided by the jet diameter gives the image scale. For the present measurements this leads to a scale of $m = 25 \pm 0.1 \, \frac{\mu m}{pixel}$. There are two reasons why the evaluation of the image scaling using the correspondence between the jet diameter to the base points of the intensity profile is not completely reliable. One reason is that the noise in the profile makes it difficult to define the exact width of the jet. The second reason is that there is an aberration at the boundary between air and oil resulting in a distortion of the image on the profile boundaries. This distortion results from the strong absorption gradient between air and oil. It occurs only at these special conditions and it is not seen on the measurement of spray where the gradients are not so strong.
The maximal spatial resolution of this system is about $10 \, \frac{\mu m}{pixel}$ which was tested by X-ray radiography of a test object (spiral-wound filament.)

3.3 Area mass

In a first analysis the sensitivity of the system, expressed through the area mass $\rho \cdot d$ can be estimated by using Eq. (3). The result is not really useful on its own because there is no information about the mass distribution in a plane through the spray, but it is indicative of the mass sensitivity. X-ray images from adhesive tape[1] with different thicknesses show that a mass sensitivity of about $1 \, \frac{mg}{cm^2}$ can be reached. This is sufficient considering the maximum area mass of the spray, which is $90 \, \frac{mg}{cm^2}$.

3.4 Density distribution

Instead of the area mass it is more useful to calculate the density distribution. Consider a situation shown in Figure 6, where a beam (r, Θ) traverses a medium with the spatially dependent attenuation coefficient $\mu\,(x, y)$. Then the attenuation can be described by the Lambert-Beer law Eq. (3). Collecting now all known variables on the left side and using the Dirac delta function we obtain the following equation

$$-\ln \frac{I\,(r, \Theta)}{I_0} = \int_{-\infty}^{\infty} \int_{-\infty}^{\infty} \mu\,(x, y)\, \delta\,(r - x\cos\Theta - y\sin\Theta)\; dx\, dy \tag{5}$$

Here the term $-\ln \frac{I(r,\Theta)}{I_0}$ is equated to the Radon transformation of the attenuation coefficient $\mu\,(x, y)$, which itself can then be calculated by the inverse Radon transformation of the left-hand side. The density is then given by

$$\rho\,(x, y) = \frac{\mu\,(x, y)}{\overline{\mu}_{Medium}} \tag{6}$$

[1] Tesafilm, comparable number and kind of atoms with the medium used here.

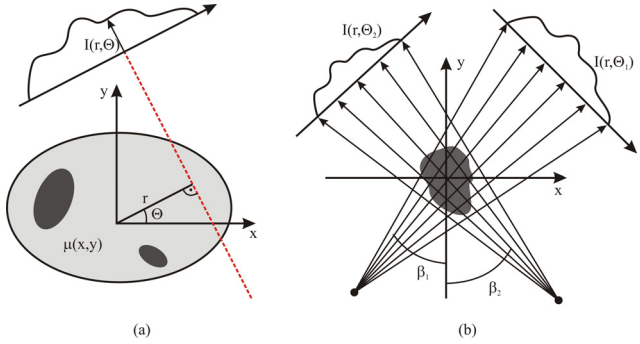

Fig. 6: Diagrammatic sketch for the attenuation of radiation in a medium (a). Rotating the observation direction for tomography (b).

For the reconstruction of the spatial density distribution, intensity profiles from different directions are required. If the observed object is axially symmetric the intensity profile is the same for all directions. But this may not be realistic for the present case. So images from different directions (Fig. 6) have been taken with the increment $\Delta\beta = 22.5°$. For normal tomography this is a large step size, but experiments have shown that for this special case it is sufficient. The process of tomography and reconstruction is described in detail in the book of Kak and Slaney [11].

3.5 Spray angle

For a simple comparison of the spray characteristics, the spray angle was estimated from the optical and the X-ray images. The approach is identically for both the optical and X-ray images because here we have an intensity distribution and the spray boundary can be defined by a threshold. Thereby the threshold is defined by a decrease of the actual intensity down to two percent of an initial intensity, which is taken to be the maximum intensity of a spray section directly at the nozzle exit. This technique is preferred here because less dense spray regions are better considered than using the FWHM-criterion (full width at half maximum).
Because the spray seems to be asymmetric, the angles are mean values from pictures from three directions.

4 EXPERIMENTAL RESULTS

In the following the results of the different measurement techniques are compared: The flow field directly at the nozzle exit, the density distribution $7\,mm$ downstream of the nozzle exit and the velocity and droplet sizes $60\,mm$ from the nozzle. An overview of all measurement positions and the definitions of coordinates and velocity directions are given in Figure 7.

4.1 Spray angle

In Table 3 the estimated spray angles from optical images and the X-ray images are shown. The optical measurements lead to a larger angle for inlay V4 and V5, whereas the angle for V4 is smallest for the X-ray angle. This can be explained by the

existence of relatively large droplets in the outer regions of the spray for V3, which are transparent in the visible range but cause a strong attenuation for the X-rays.

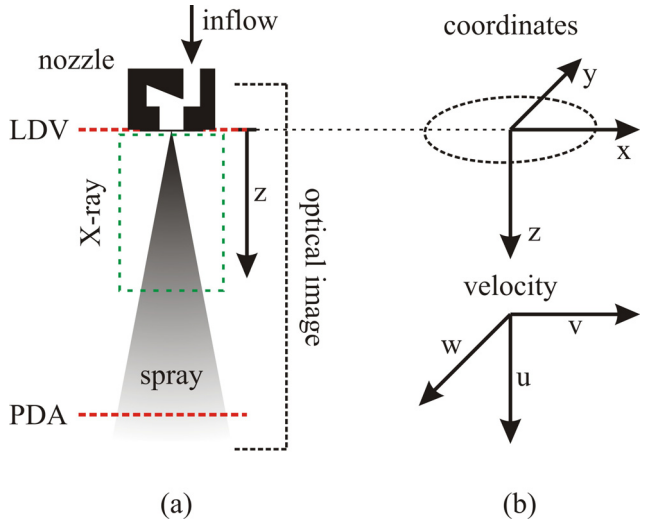

Fig. 7: Measurement positions and definition of coordinates and velocity directions.

In V5 the optical angle exceeds the value of the X-ray measurements by 25 %. This can be explained by the existence of many very small droplets in the spray of V5: this droplet cloud is opaque for visible light but the cumulative mass is too low for a measureable attenuation of the X-rays.

Tab. 3: Spray angle calculated from optical and X-ray images.

image type	VD	V3	V4	V5
optical	0.0°	4.3°	5.6°	10.8°
X-ray	0.0°	5.0°	4.8°	8.1°

4.2 PDA measurements in the spray

Figure 8 presents the axial mean velocity, the mean droplet diameter D_{10} and the data rate in the spray 60 mm downstream from the nozzle exit. All sprays have a Gaussian shaped velocity profile. Inlay V3 has the highest maximum velocity and V5 the widest profile.
The mean droplet diameter distribution shows a significant increase in the center of the spray for V3 and V4 caused by non-spherical ligaments. For V5 the mean diameters are relatively low compared to the other inserts and the increase in the center is marginal. In the outer spray regions the mean droplet diameters for V4 and V5 are nearly equal and clearly smaller then those of V3. The increase of the diameters on the right side, especially in case of V5, are due to the longer path length through the spray to the receiving optic, since scattered light from the smaller particles cannot penetrate the spray.
The position of the maximum data rates underline the enhanced breakup of inlay V5. Again the higher data rates on the left can be explained by the shorter path length to the receiving optics. Additionally the enhanced breakup on the left side of the spray of V5 also arguments the data rate.

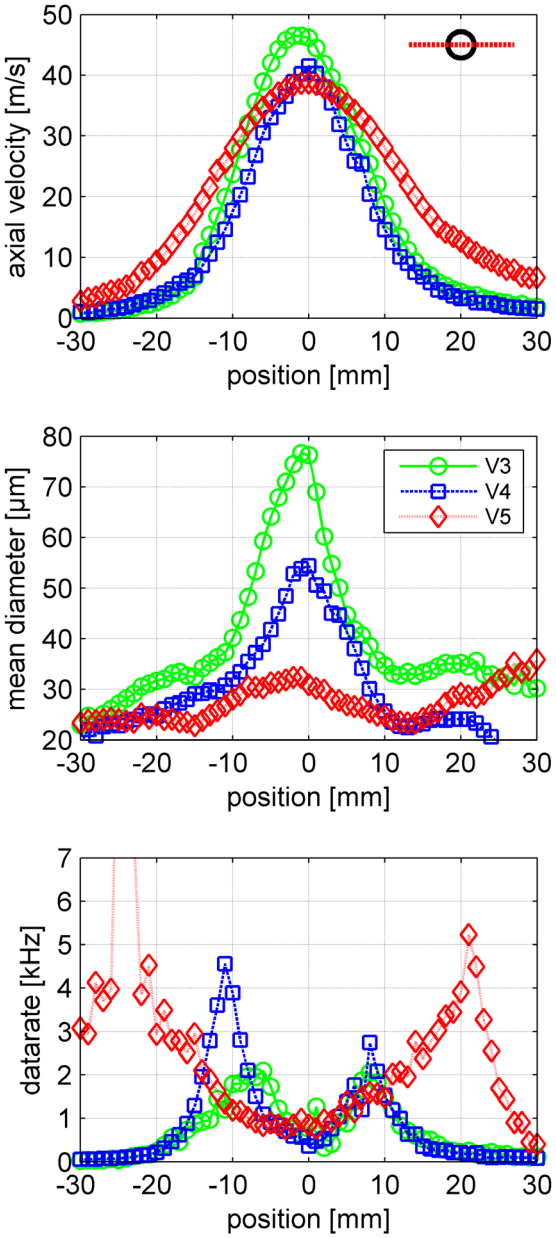

Fig. 8: Axial mean velocity, mean droplet diameter D_{10} and data rate for cross section in x-direction at 60 mm distance from the nozzle exit.

4.3 Density development

Figure 9 shows the density development in the spray on the centre line. For comparison the mean density calculated from the mean spray angle (optical and X-ray) and assuming radial symmetry is also shown. The values for the inlays V3 and V4 are all greater than the mean values, whereas the values for inlay V5 are identical with the mean values for a nozzle distance higher than 10 mm. For smaller distances the values for V5 are lower than the mean values. The reason for this is that here the maximum density in a section is not on the centre line. Finally this comparison for inlay V5 shows that for a nozzle distance greater than 10 mm the density is homogeneous over the area defined by the spray angle. V3 reaches the same situation for a significant larger distance of about 16 mm and for V4 the density in the observed area is still higher.

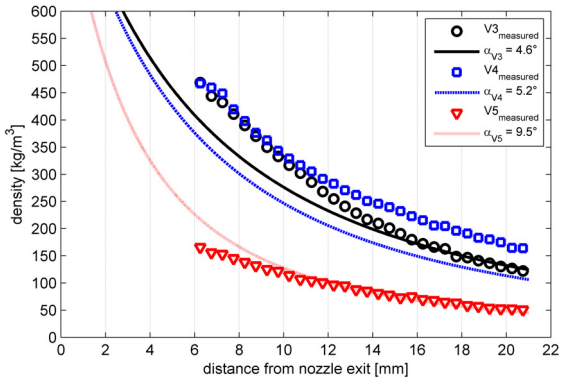

Fig. 9: Density development in the spray on the centre line compared with the mean density distribution calculated from the mean spray angle.

4.4 Density distribution and nozzle flow

In Figure 10 the axial velocity, the cross-flow velocity and the turbulence level at the nozzle exit, as well as the density distribution in the spray at 7 mm downstream of the nozzle exit are shown for the reference nozzle and all inlays. The axial velocity of the base nozzle exhibits nearly rotational symmetry. At certain points in the cross velocity distribution there are small values caused by a very small angle between nozzle, transmitting and receiving optics. However this indicates that the measurements and the evaluation procedure are reliable.
Comparing the axial velocities from the different inlays with the density distribution in Figure 10 there is no directly visible similarity.
The cross-flow velocity exhibits two vortices in the flow of V3. In the density distribution of this inlay there is a structure which looks similar to the two vortices but rotated by 45°. In the case of V4 the mean flow is directed to the left, where the density distribution is maximal. Such a cross-flow is not impossible, considering that the cross-flow velocities are very small compared to the axial velocity.

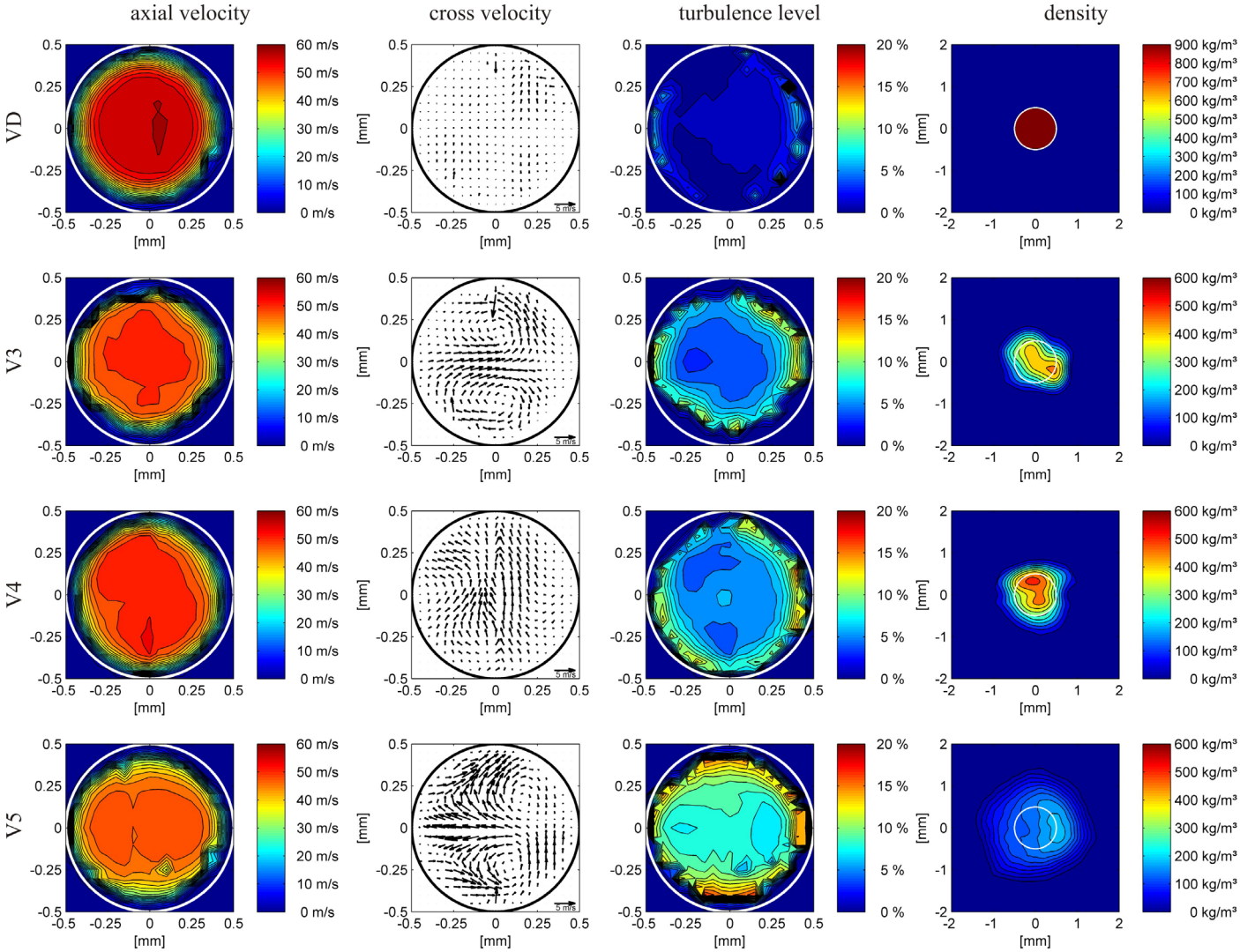

Fig. 10: Axial velocity, cross velocity and turbulence level at the nozzle exit and density distribution 7 mm below nozzle exit for the reference nozzle VD and the inlays V3, V4 and V5. Density distribution for the inlays are scaled with a maximum density of 600 $\frac{kg}{m^3}$ instead of the medium density for clarity.

On the left side of V5 there are two strong vortices visible with a very high velocity directed towards the nozzle wall, whereas on the other side there is a relatively undisturbed area. Compared to the density distribution on the left side there is also significantly better breakup and on the right a relatively solid area. So here the cross velocity apparently promotes breakup.
The plots for the turbulence level calculated with Eq. (7) show that there are higher values at the boundary. Comparing the distribution of the inlays with each other it can be seen that the increased turbulence levels correspond to larger spray angles.

4.5 Turbulence and RMS

With respect to the velocity distribution a comparison only in a longitudinal section through the nozzle section might be not informative so we have estimated a mean turbulence level Eq.(7) over the cross section in the nozzle for each inlay.

$$Tu = \sqrt{\frac{\overline{u'^2} + \overline{v'^2} + \overline{w'^2}}{3 \cdot \left(\overline{u}^2 + \overline{v}^2 + \overline{w}^2\right)}} \tag{7}$$

As seen in Table 4 the mean turbulence level increases from the reference nozzle to V3, V4 to V5, thus in the same order as the spray angle increases in the optical measurements.
To see the influence of the cross-flow RMS we calculated the ratio between the RMS of one direction and the total RMS. Equation (8) shows the expression for the axial component.

$$R_{u'} = \sqrt{\frac{\overline{u'^2}}{\overline{u'^2} + \overline{v'^2} + \overline{w'^2}}} \tag{8}$$

The results are shown in Table 4. First it can be seen that the values for the cross components $R_{v'}$ and $R_{w'}$ are nearly equal and they are also all lower than the axial value $R_{u'}$. Only in the case of the reference nozzle VD is the ratio for both cross-flow values $R_{v'+w'}$ higher than the axial value $R_{u'}$. Comparing the values between V3 and V4 there are only small differences, whereas in the mean turbulence level (Tu), inlay V4 leads to a higher value than V3. For the last inlay the ratio for the cross-flow components is higher than those from inlays V3 and V4 and the axial component is accordingly lower.
In summary, a higher overall turbulence level (Tu) leads to a stronger primary breakup (compared with Fig. 3); however closer examination shows that this is not true for the fluctuation level of the axial velocity. The stronger breakup appears to be related more to the increased fluctuations of the cross-flow velocity components.

Tab. 4: Mean turbulence levels for the investigated geometries and the ratio of the RMS.

	VD	V3	V4	V5	
Tu	1.59	5.25	6.26	8.45	$[\%]$
$R_{u'}$	5.49	8.16	8.23	7.68	$[\cdot 10^3]$
$R_{v'}$	4.99	3.60	3.51	3.96	$[\cdot 10^3]$
$R_{w'}$	4.27	3.48	3.40	4.11	$[\cdot 10^3]$
$R_{v'+w'}$	6.85	5.12	4.96	5.93	$[\cdot 10^3]$

5 CONCLUSIONS

1. For four different nozzle geometries the flow field at the nozzle exit, the density distribution of the spray near the nozzle exit as well as the velocity and droplet diameters in the spray have been measured.

2. With X-ray tomography it was possible to achieve the density distribution in the optical opaque spray near the nozzle exit.

3. Differences between the spray angle evaluated out of optical and X-ray images can yield information about the existence of small droplets in the outer regions of the spray.

4. It was observed that high cross-flow velocities seem to enhance the breakup.

5. Higher mean turbulence levels produce more smaller droplets for the same ratio of cross-flow RMS compared to the axial RMS.

6. A higher fraction of the cross-flow RMS compared to the axial RMS leads to improved breakup.

7. In future, the same geometries will be investigated with another medium to reach higher Reynolds numbers in order to obtain a better comparability with real diesel conditions.

6 ACKNOWLEDGMENT

The authors would like to thank Walter Bauer from the Robert Bosch GmbH for the development of the X-ray measurement facility and the support in the X-ray measurements.

7 NOMENCLATURE

Symbol	Quantity	SI Unit
a, b	constants	$\frac{m^2}{s^2}, -$
b_{slit}	slit size PDA receiving optic	μm
D	approach diameter	mm
D_{10}	mean droplet diameter	μm
d	nozzle diameter	mm
d_m	measurement volume diameter	μm
I, I_0	intensity of optical and X-ray images	$-$
L	nozzle length	mm
l_m	measurement volume depth	μm
m	image scale	$\frac{\mu m}{pixel}$
p	pressure	Pa
q	volume flux	$\frac{m^3}{s}$
R	ratio of RMS to whole RMS	$-$
r	radius	μm
s	distance	m
T	temperature	K
Tu	turbulence level	$\%$
u, v, w	velocity in x,y,z direction	$\frac{m}{s}$
u', v', w'	RMS in x,y,z direction	$\frac{m}{s}$
x, y, z	coordinates	$-$

Symbol	Quantity	SI Unit
β	step angle for tomography	$^\circ$
δ	Dirac delta function	$-$
ρ	density	$\frac{kg}{m^3}$
Θ	angle in tomography	$^\circ, rad$
ϑ	angle for LDV and PDA	$^\circ$
μ	spatially dependent attenuation coefficient	$\frac{1}{m_2}$
$\overline{\mu}$	attenuation coefficient	$\frac{m^2}{kg}$

8 REFERENCES

[1] N. Tamaki and M. Shimizu, *Effects of Cavitation and Internal Flow on Atomization of a Liquid Jet*, Atomization and Sprays, Vol. 8, pp. 179–197, 1998.

[2] H. Hiroyasu, *Spray Breakup Mechanism from the Hole-Type Nozzle and its Application*, Atomization and Sprays, Vol. 10, pp. 511–527, 2000.

[3] L.C. Ganippa, G. Bark, S. Andersson, and J. Chomiak, *The Structure of Cavitation and its Effect on the Spray Pattern in a Single-Hole Diesel Nozzle*, Society of Automotive Engineers, 2001-01-2008, 2000.

[4] A. Sou, M.I. Maulana, S. Hosokawa, and A. Tomiyama, *Cavitation in Cylindrical Nozzles and Two-Dimensional Nozzles*, 6th International Conference on Multiphase Flow (ICMF), Leipzig, Germany, 2007.

[5] C. Badock, *Untersuchung zum Einfluß der Kavitation auf den primären Strahlzerfall bei der dieselmotorischen Einspritzung* , Ph.D. Thesis, Technische Universität Darmstadt, 1999.

[6] M. Stahl, N. Damaschke, and C. Tropea, *Experimental Investigation of Turbulence and Cavitation inside a Pressure Atomizer and Optical Characterization of the Generated Spray*, Proc. of the ICLASS 2006, Kyoto, Japan, ICLASS06-116, 2006.

[7] K. Heukelbach, *Untersuchung zum Einfluss der Düseninnenströmung auf die Stabilität flächiger Flüssigkeitsstrahlen*, Ph.D. Thesis, Technische Universität Darmstadt, 2003.

[8] J. Walther, *Quantitative Untersuchung der Innenströmung in kavitierenden Dieseleinspritzdüsen*, Ph.D. Thesis, Technische Universität Darmstadt, 2002.

[9] M. Fischer, *Turbulente wandgebundene Strömungen bei kleinen Reynoldszahlen*, Ph.D. Thesis, Universität Erlangen-Nürnberg, 2000.

[10] H.-E. Albrecht, M. Borys, N. Damaschke, and C. Tropea, *Laser Doppler and Phase Doppler Measurement Techniques*, Springer Verlag, Heidelberg, 2003.

[11] Kak and M. Slaney, *Principles of Computerized Tomographic Imaging*, Society of Industrial and Applied Mathematics, 2001.